



Validation of the plasma-wall interaction simulation code ERO2.0 by the analysis of tungsten migration in the open divertor region in the Large Helical Device

M. Shoji^{a,b,*}, G. Kawamura^{a,b}, J. Romazanov^c, A. Kirschner^c, S. Masuzaki^{a,b}, M. Tokitani^{a,b}, S. Brezinsek^c

^a National Institute for Fusion Science, National Institutes of Natural Sciences, 322-6 Oroshi-cho, Toki 509-5292, Japan

^b The Graduate University for Advanced Studies (SOKENDAI), Shonan Village, Hayama 240-0913, Japan

^c Forschungszentrum Jülich GmbH, Institut für Energie- und Klimaforschung - Plasmaphysik, Partner of the Trilateral Euregio Cluster (TEC), Jülich 52425, Germany

ARTICLE INFO

Keywords:

ERO2.0

Tungsten migration

Plasma-wall interaction

EMC3-EIRENE

LHD

ABSTRACT

Tungsten migration in the open divertor region in the Large Helical Device is analyzed for validating the three-dimensional plasma-wall interaction simulation code ERO2.0. The ERO2.0 simulation reproduced the measurement of localized tungsten migration from a tungsten-coated divertor plate installed in the inboard side of the torus. The simulation also explained the measurement of the high tungsten areal density in the private side on a carbon divertor plate, next to the tungsten-coated divertor plate, by the tungsten prompt redeposition in plasma discharges for a low magnetic field strength in a counterclockwise toroidal direction. However, the simulation disagreed with the measurement of low tungsten areal density on the plasma-wetted areas on the carbon divertor plates, which indicated that the actual erosion rate of the redeposited tungsten should be much higher than that used in the ERO2.0 code.

Introduction

The understanding of material migration is one of the critical issues for future nuclear fusion reactors to estimate the lifetime of plasma-facing materials (PFMs), reduce the tritium inventory contained in impurity deposition layers on the PFMs, and control particle fueling from the deposition layers, etc. Tungsten is considered the most promising material for plasma-facing components (PFCs) because of its low tritium retention, high melting point, low erosion rate, etc [1,2]. In a previous experimental campaign in the Large Helical Device (LHD) [3], tungsten migration was investigated in the open divertor region by replacing a conventional carbon (isotropic graphite) divertor plate with a tungsten-coated plate manufactured using vacuum plasma spray (VPS) method, which was installed near the equatorial plane in the inboard side of the torus. After the experimental campaign, several carbon divertor plates near the tungsten divertor plate were retrieved, and a post-mortem analysis of the surface was performed using the simultaneous ion beam measurement technique of Rutherford backscattering spectroscopy (RBS) and elastic recoil detection (ERD) [4]. The measurements of

the tungsten areal density profile on the carbon divertor plates showed that the migration of tungsten was localized near the tungsten divertor plate along the right divertor plate array. The measured tungsten density profile along the direction perpendicular to that of the divertor plate array demonstrated higher tungsten areal density in the private side on a carbon divertor plate installed next to the tungsten divertor plate, and quite low tungsten densities on the plasma-wetted areas. These observations can contribute to the understanding of the physical mechanism of tungsten migration in the divertor region in the LHD. For the interpretation of the observed tungsten areal density profile, the three-dimensional Monte-Carlo plasma-wall interaction (PWI) and impurity transport simulation code ERO2.0 [5] has been applied. The ERO2.0 code has several advantages over the other PWI codes in managing the effect of the Larmor radius of sputtered tungsten, the change of the materials on the PFCs caused by PWI processes, the effect of the chemical sputtering of carbon, and so on. Additionally, the code provides the density profile of impurities in the peripheral plasma being consistent with the rate of PWI processes on the divertor plates. In section 2, the setup for the ERO2.0 code for investigating the tungsten migration is

Abbreviations: LHD, The Large Helical Device.

* Corresponding author.

E-mail addresses: shohji.mamoru@nifs.ac.jp, shoji@nifs.ac.jp (M. Shoji).

<https://doi.org/10.1016/j.nme.2022.101257>

Received 30 June 2022; Received in revised form 26 August 2022; Accepted 15 September 2022

Available online 16 September 2022

2352-1791/© 2022 The Authors. Published by Elsevier Ltd. This is an open access article under the CC BY-NC-ND license (<http://creativecommons.org/licenses/by-nc-nd/4.0/>).

presented. In section 3, the simulation results of the tungsten flux density profile on the divertor plates near the tungsten divertor plate in different magnetic field configurations are shown. In section 4, the ERO2.0 simulation of the integrated tungsten areal density profile in the previous experimental campaign is compared with the measurements at several positions on the retrieved carbon divertor plates, which is for validating the ERO2.0 simulation.

Setup for the simulation of tungsten migration in the open divertor region using the ERO2.0 code

Fig. 1 shows a three-dimensional grid model for analyzing the tungsten migration in the divertor region for the ERO2.0 code. This model is for the simulation in the open divertor configuration for one helical pitch angle (36° in toroidal direction), in which a periodic boundary condition is assumed at both toroidal ends. In this simulation, the trajectories of many test particles (about 5 million), which are representatives of impurities generated on the divertor plates, are tracked by using the database on plasma-wall interactions calculated by SDTrimSP [6], and the database on atomic-molecular processes (ADAS) [7] under a fixed background (hydrogen) plasma. The three-dimensional plasma parameter profiles are defined between an inner plasma boundary and the outer edge of the plasma, including divertor legs. The profiles are provided by a three-dimensional edge plasma simulation code (EMC3-EIRENE) with a fixed boundary condition of the plasma heating power ($P_{\text{LCFS}}^{\text{LH}}$) and plasma density (n_e^{LCFS}) at the inner plasma boundary, just inside the Last Closed Flux Surface (LCFS) [8,9]. The energy and the particle diffusion coefficients in the plasma are assumed to be 1.0 and $0.5 \text{ m}^2/\text{s}$, respectively, which are typical values for explaining the measurements of the radial profile of the electron temperature and the plasma density in the peripheral plasma.

In this grid model, the vacuum vessel and the divertor plates consist of the aggregation of small triangles (a few centimetres in dimension). It is assumed that the surface of the vacuum vessel is fully covered with carbon, which is experimentally supported by a colourimetric analysis [10]. A divertor plate installed near the equatorial plane in the inboard side of the torus, which is one of the plates installed along the right divertor plate array, is set to be a tungsten plate (shown as blue grids in Fig. 1). The other divertor plates are composed of carbon (indicated as black grids in Fig. 1). The shape and position of the PFCs are set to reproduce the actual configuration in the previous experimental campaign in the fiscal year 2008. The temperature of all divertor plates is assumed to be 600 K, which is a typical temperature during plasma discharges. The Homogeneous Mixing Model (HMM) [11] was applied, in which the thickness of the interaction layer on the surface of the carbon divertor plates was $0.1 \text{ }\mu\text{m}$, which corresponded to the

representative depth of the tungsten concentration on a carbon plate near the tungsten divertor plates in the JT-60U [12]. The thickness of the interaction layer on the tungsten divertor was assumed to be 1 nm, which was determined with reference to a Molecular Dynamics (MD) simulation of the depth profile of cumulative carbons on crystalline tungsten bulk [13].

It has been recognized that the dominant process of erosion on the tungsten divertor plates in LHD plasmas is the physical sputtering caused by incident carbon ions in the peripheral plasma (not by hydrogen ions) because of the much higher physical sputtering rate of tungsten by carbon ions [6]. The net tungsten deposition profile, in which the eroded tungsten is subtracted from the deposited tungsten, is calculated using the so-called 'global modeling approach' in the ERO2.0 simulation, in which the erosion of tungsten by carbon ions is obtained in a self-consistent way, using the calculated incident flux of the carbon ions onto the tungsten divertor plate (the concentration of the carbon ions in the peripheral plasma is not artificially assumed). A steady-state solution of the net tungsten deposition profile is obtained after multiple iteration steps in which the PWI and the impurity transport calculation parts in the ERO2.0 code interact with each other. In the 0th step, the test particles (representatives of carbon ions/atoms and hydrocarbons) are created on the carbon divertor plates by the physical and chemical sputtering due to the hydrogen ions in the background peripheral plasma. The trajectories of the test particles are traced until they hit PFCs such as the vacuum vessel and the divertor plates, by which the flux density profile of the test particles on the PFCs is calculated by adding up the profile for all test particles. In the first step, the test particles additionally include tungsten and carbon created by the sputtering on the PFCs in the previous step. The test particles cause not only physical/chemical sputtering but also self-sputtering on the PFCs. By repeating these iteration steps, tungsten and carbon flux density profiles are converged, in which the negative and positive flux densities mean the erosion and deposition rate of the test particle material. The iterative calculation finally produces a steady-state profile of the erosion and deposition rate on the PFCs. In this simulation, the length of time for each iteration step was set to one second. The ERO2.0 simulations for the tungsten migration analysis prove that the carbon flux density on the divertor plates increases with the iteration step to finally converge at around the fifth step, and that the tungsten flux density also converges. Thus, the simulations in the fifth step are presented hereafter in this paper. In the ERO2.0 simulation, it is assumed that deposited tungsten and carbon form pure solid deposition layers which do not have amorphous-like structures and do not contain any other materials.

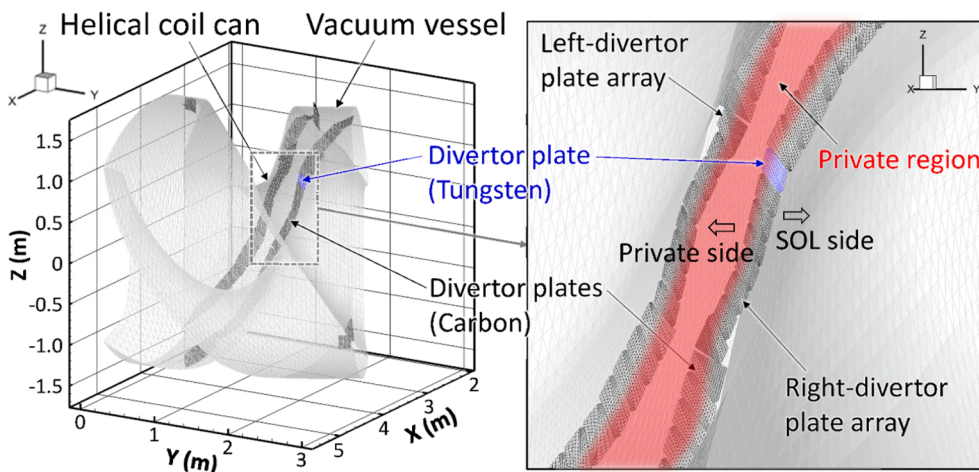


Fig. 1. A three-dimensional grid model for analyzing the tungsten migration in the open divertor region in the LHD for one helical pitch angle (36° in toroidal direction) for the ERO2.0 simulation, which is viewed from the outboard side of the torus. The right figure is an enlarged view of the divertor plate array installed in the inboard side of the torus. The private region is shown as a transparent red area between the left and right divertor plate arrays. The tungsten-coated divertor plate is indicated as blue grids. (For interpretation of the references to colour in this figure legend, the reader is referred to the web version of this article.)

The effect of the magnetic field strength and the toroidal direction on the net tungsten flux density profile on the carbon divertor plates

The magnetic field configuration in front of tungsten divertor plates strongly affects the tungsten migration, such as the so-called “prompt redeposition”. The tungsten migration near the tungsten-coated divertor plate was investigated for a plasma discharge condition ($P^{LCFS} = 2$ MW, $n_e^{LCFS} = 1 \times 10^{19} \text{ m}^{-3}$) under a magnetic field configuration $R_{ax} = 3.60$ m (R_{ax} is the position of the magnetic axis in the major radius), which was the most frequent experimental condition for plasma discharges in the previous experimental campaign. It has been found that the ERO2.0 simulations show higher tungsten erosion rates in this magnetic field configuration, compared to those in the others (such as $R_{ax} = 3.75$ and 3.90 m), because of the high ion flux density in the inboard side of the

torus for $R_{ax} = 3.60$ m [14]. Fig. 2 illustrates the net tungsten flux density profile on the carbon divertor plates installed along the right divertor plate array for high, medium, and low magnetic field strengths in clockwise (positive) and counterclockwise (negative) toroidal magnetic field directions. The typical electron temperature and plasma density on the tungsten divertor plate are ~ 30 eV and $\sim 3 \times 10^{17} \text{ m}^{-3}$ in this simulation, respectively. Fig. 2 (a) and (b) display the net tungsten flux density profile for the high magnetic field strength in the positive and negative toroidal directions ($B_t = +2.75$ and -2.75 T), respectively. The simulations in both cases are almost identical, which is because of the quite larger angle between the magnetic field lines and the surface of the divertor plates compared to that in tokamaks [15]. In the medium magnetic fields ($B_t = +1.50$ and -1.50 T), this situation is not significantly changed, as shown in Fig. 2 (c) and (d), respectively. However, in the low magnetic fields ($B_t = +0.50$ and -0.50 T), the situation is quite

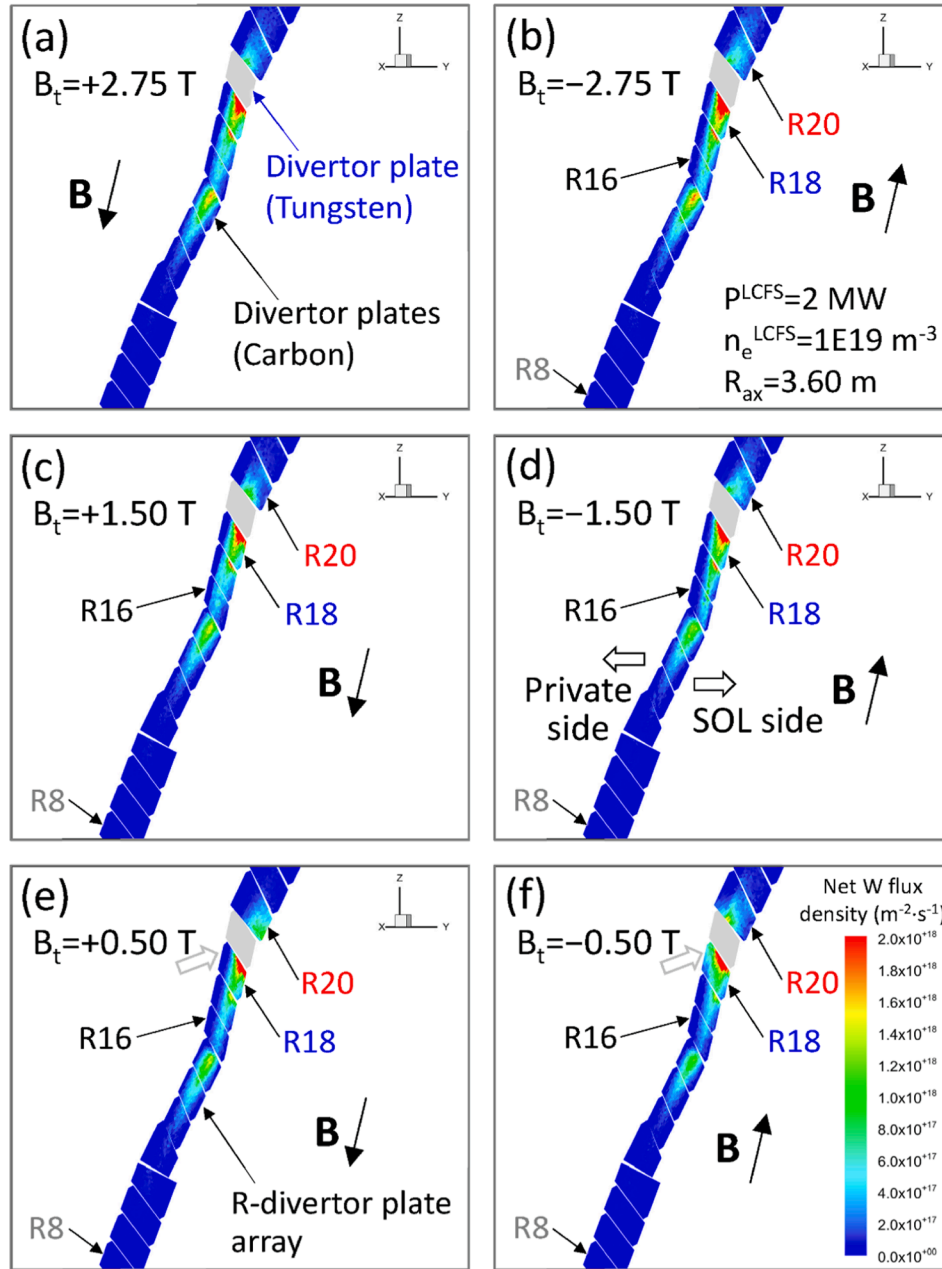


Fig. 2. The simulations of the net tungsten flux density profile on the carbon divertor plates, installed along the right divertor plate array in the inboard side, for high ($B_t = +2.75$ (a) and -2.75 T (b)), medium ($B_t = +1.50$ (c) and -1.50 T (d)), and low ($B_t = +0.50$ (e) and -0.50 T (f)) magnetic field strengths in the two different (clockwise and counterclockwise) toroidal magnetic field directions for $P^{LCFS} = 2$ MW, $n_e^{LCFS} = 1 \times 10^{19} \text{ m}^{-3}$, and $R_{ax} = 3.60$ m.

different. The simulation of the net tungsten flux density profile for the low magnetic field strength in the positive toroidal direction differs from that in the negative toroidal direction, especially on a divertor plate installed next to the tungsten divertor plate (named “R18”), which is indicated by an open grey arrow in Fig. 2 (e) and (f). The figures show that the net tungsten flux density in the private side on the divertor plate “R18” for $B_t = -0.50$ T is much higher than that for $B_t = +0.50$ T. This difference was explained by the prompt redeposition of tungsten ions in the peripheral plasma (the divertor leg) which are produced by the ionization of sputtered tungsten atoms on the tungsten divertor plate.

Fig. 3 (a) and (b) illustrate the representative trajectories of tungsten atoms/ions produced by physical sputtering on the tungsten divertor plate for both toroidal magnetic field directions ($B_t = +0.50$ and -0.50 T), respectively. The three-dimensional trajectories of tungsten atoms/ions which deposit on the carbon divertor plate “R18” are indicated as coloured lines. The average kinetic energy of the sputtered tungsten atoms was ~ 12 eV, which provides an average mean free path of the tungsten atoms of ~ 40 mm in the typical plasma parameters on the tungsten divertor plate. In the low magnetic field cases (~ 0.2 T at the divertor plate), the average Larmor radius of the singly ionized tungsten ions was ~ 34 mm. The mean free path and the Larmor radius reasonably explain the difference in the net tungsten flux density profile on the divertor plate “R18” for the low magnetic fields by the prompt redeposition. As for the tungsten deposition in the private side by the effect of the $E \times B$ drift, this effect is insignificant because of the low electric field in the divertor legs due to the small gradient of the electron temperature (short connection lengths of the magnetic field lines in this region).

Fig. 4 gives the simulations of the net carbon flux density profiles on the carbon divertor plates along the right divertor plate array for the high, medium, and low magnetic field strengths in the positive and negative toroidal magnetic field directions. The erosion areas, in which the net carbon flux density is negative, are dominant on the divertor plates, and the maximum erosion rate (corresponding to the absolute minimum net carbon flux density) is higher than that of the deposition rate (the maximum net carbon flux density) by about one order of magnitude. The simulations can also be used as a good reference for the distribution of the plasma-wetted areas on which the materials on the divertor plates are eroded by incident ions in the peripheral plasma. The simulations show that the carbon flux density profiles are not significantly changed in all magnetic field configurations. In addition, the total erosion rate of carbons sputtered by the background peripheral plasma and the impurities at the 0th step is almost the same under all magnetic conditions. This is because of the small Larmor radii of carbon and hydrogen ions which cause the erosion on the carbon divertor plates. It should be noted that the absolute value of the negative carbon flux

density on the plasma-wetted areas is much higher than that of the tungsten flux density in these areas (shown in Fig. 2) by about two orders of magnitude, which means that the erosion is dominant in the plasma wetted areas on the divertor plates, even in the position near the tungsten divertor plate. The ERO2.0 simulations indicate that the carbon tends to deposit in the private side on the right divertor plate array (corresponding to the left side in Fig. 4 (a-f)). It has been revealed that the remaining sputtered carbon is transported to the vacuum vessel near the carbon divertor plates [16].

Comparison of the simulation of the integrated net tungsten density profile with the measurement in the previous experimental campaign

The ERO2.0 code can calculate the density profile of tungsten deposited on the carbon divertor plates in each plasma discharge condition by multiplying the tungsten flux density by the plasma discharge time. By summing up the tungsten density profiles in all plasma discharge conditions in the previous experimental campaign, the integrated tungsten density profile can be compared with the measurement. It should be noted that the history of the operational condition of the plasma discharges is not considered in this analysis. The total plasma discharge time in the previous experimental campaign was distinguishable according to the plasma heating power P^{LCFS} , the plasma density n_e^{LCFS} , the radial position of the magnetic axis R_{ax} , and the magnetic field strength and the toroidal direction B_t . These four parameters (P^{LCFS} , n_e^{LCFS} , R_{ax} , and B_t) were classified by five plasma heating powers ($P^{LCFS} = 1, 2, 4, 6$, and 8 MW), five plasma densities ($n_e^{LCFS} = 1, 2, 4, 6$, and $8 \times 10^{19} \text{ m}^{-3}$), three magnetic axis positions ($R_{ax} = 3.60, 3.75$, and 3.90 m), and six toroidal magnetic fields ($B_t = \pm 0.50, \pm 1.50$, and ± 2.75 T (± 2.50 T for $R_{ax} = 3.90$ m)), respectively. This classification indicated that the total plasma discharge times for $R_{ax} = 3.60$ m with the high magnetic fields ($B_t = +2.75$ and -2.75 T) were dominant (about 4,000 s and 2,700 s, respectively), which were followed by that for $R_{ax} = 3.75$ m with the medium magnetic field ($B_t = +1.50$ T) (about 1,300 s). It was found that the plasma discharge time for $R_{ax} = 3.60$ m with the low magnetic field ($B_t = -0.50$ T) was relatively long (about 600 s), which contributed to the tungsten flux density in the private side on the carbon divertor plate “R18”, as indicated in Fig. 3(b). It was also found that the plasma discharge time in the lower plasma heating powers of $P^{LCFS} = 1 \sim 2$ MW and a plasma density of $n_e^{LCFS} = 1 \times 10^{19} \text{ m}^{-3}$ was dominant in all magnetic field configurations (R_{ax} and B_t).

Fig. 5 (a) presents the calculated net tungsten density profile along the right divertor plate array, which was obtained by integrating net tungsten flux densities in various plasma discharge conditions multiplied by the plasma discharge times in each condition. The simulation

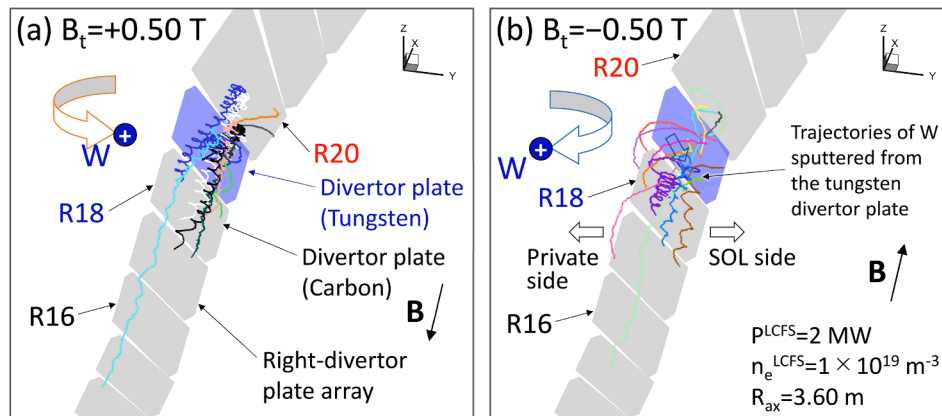


Fig. 3. The representative trajectories (indicated as coloured lines) of tungsten atoms and ions produced by physical sputtering on the tungsten-coated divertor plate (shown as a transparent blue plate) for the low magnetic fields ($B_t = +0.50$ (a) and -0.50 T (b)) calculated by the ERO2.0 code for $P^{LCFS} = 2$ MW, $n_e^{LCFS} = 1 \times 10^{19} \text{ m}^{-3}$, and $R_{ax} = 3.60$ m. (For interpretation of the references to colour in this figure legend, the reader is referred to the web version of this article.)

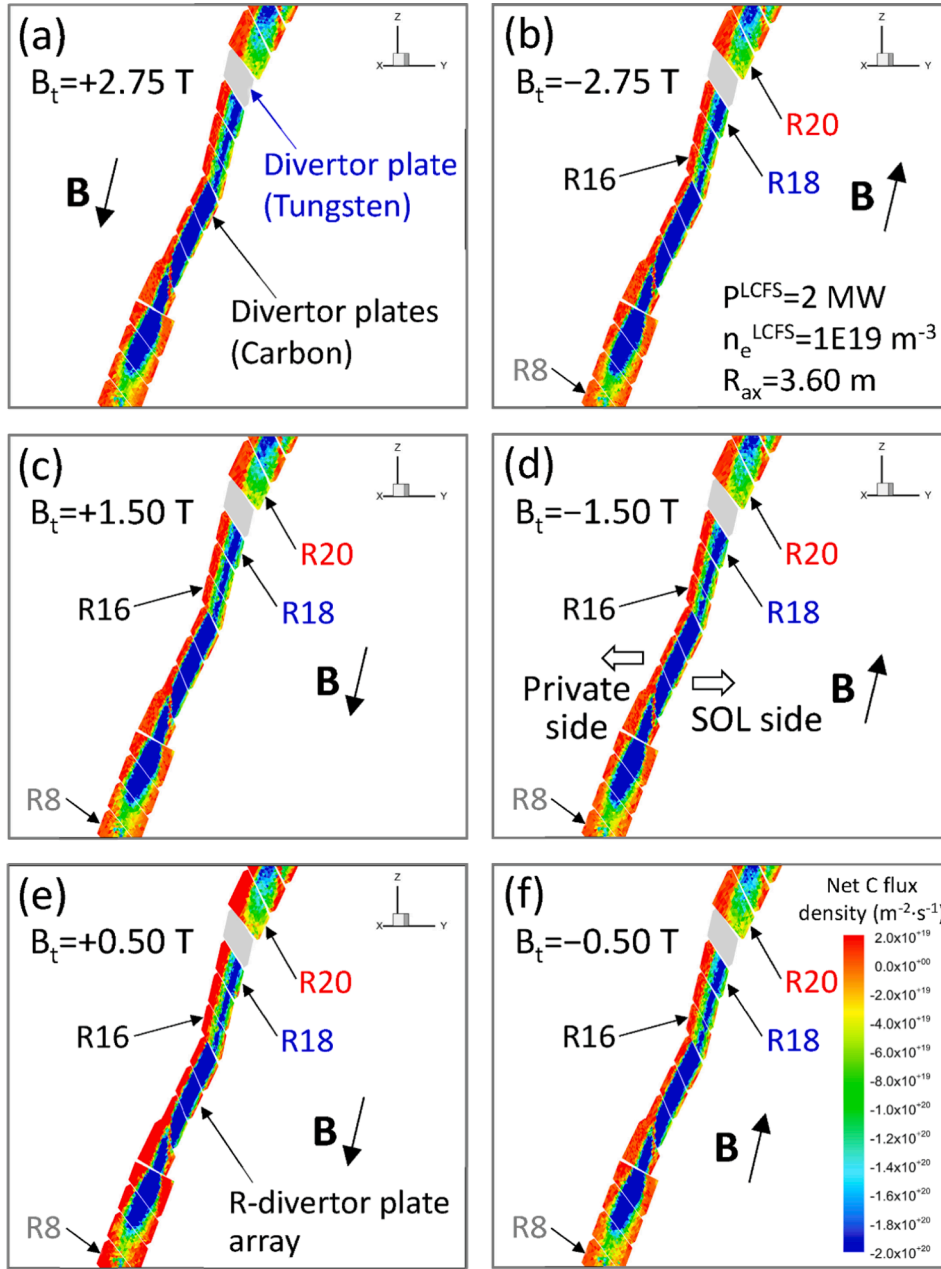


Fig. 4. The simulations of the net carbon flux density profiles on the carbon divertor plates, installed along the right divertor plate array in the inboard side, for high ($B_t = +2.75$ (a) and -2.75 T (b)), medium ($B_t = +1.50$ (c) and -1.50 T (d)), and low ($B_t = +0.50$ (e) and -0.50 T (f)) magnetic field strengths in the two different (clockwise and counterclockwise) toroidal magnetic field directions for $p^{\text{LCFS}} = 2$ MW, $n_e^{\text{LCFS}} = 1 \times 10^{19} \text{ m}^{-3}$, and $R_{\text{ax}} = 3.60$ m. It should be noticed that the range of the colour bar is different from that in Fig. 2.

shows that tungsten sputtered from the tungsten divertor plate was transported downward, which corresponds to the plasma flow along the magnetic field lines in the divertor leg connecting to the right divertor plate array. Fig. 5 (a) also demonstrates that the sputtered tungsten locally deposits near the tungsten divertor plate. Fig. 5 (b) displays the simulation of the integrated net tungsten areal density profile along lines on four carbon divertor plates ("R20", "R18", "R16", and "R8"), which are indicated as black lines in Fig. 5 (a). The values on the abscissa in Fig. 5 (b) mean the distance from the edge of the corner of the divertor plate in the private side. The ERO2.0 simulation shows quite low tungsten density on the divertor plate "R8", which position was relatively far from the tungsten divertor plate. The simulation also presents that the tungsten density in the private side on the carbon divertor plate "R18", which position was next to the tungsten divertor plate, is higher than that in the private side on the other divertor plates (the position is indicated with open grey arrows in Fig. 5 (a) and (b)).

Table 1 presents the measured tungsten areal density in the previous experimental campaign at three positions ("a", "b", and "c") on the four

carbon divertor plates which correspond to the retrieved divertor plates after the previous experimental campaign. The positions are marked with small white circles on the black lines in Fig. 5 (a). Positions "a", "b", and "c" correspond to the edge of the corner of the divertor plate in the private side, the positions apart from the edge by ~ 40 mm and ~ 100 mm, respectively. Position "c" is just in the plasma-wetted areas on the divertor plates, which are the erosion dominant areas shown as blue or green on the carbon divertor plates in Fig. 4. The measured tungsten areal densities are plotted in Fig. 5 (b) as red circles. It should be noted that the measured tungsten areal density in the private side on the carbon divertor plate "R18" is higher than that on the other divertor plates. This high tungsten areal density in the private side (position "a") on this divertor plate is qualitatively reproduced by ERO2.0, which is explained by the migration of tungsten sputtered from the tungsten divertor plate in the plasma discharges for $R_{\text{ax}} = 3.60$ m in the low magnetic field strength in the negative toroidal direction ($B_t = -0.50$ T), as schematically shown in Fig. 3 (b). The measured low tungsten areal density on the divertor plates "R8" (positions "a-c" of "R8" in Table 1)

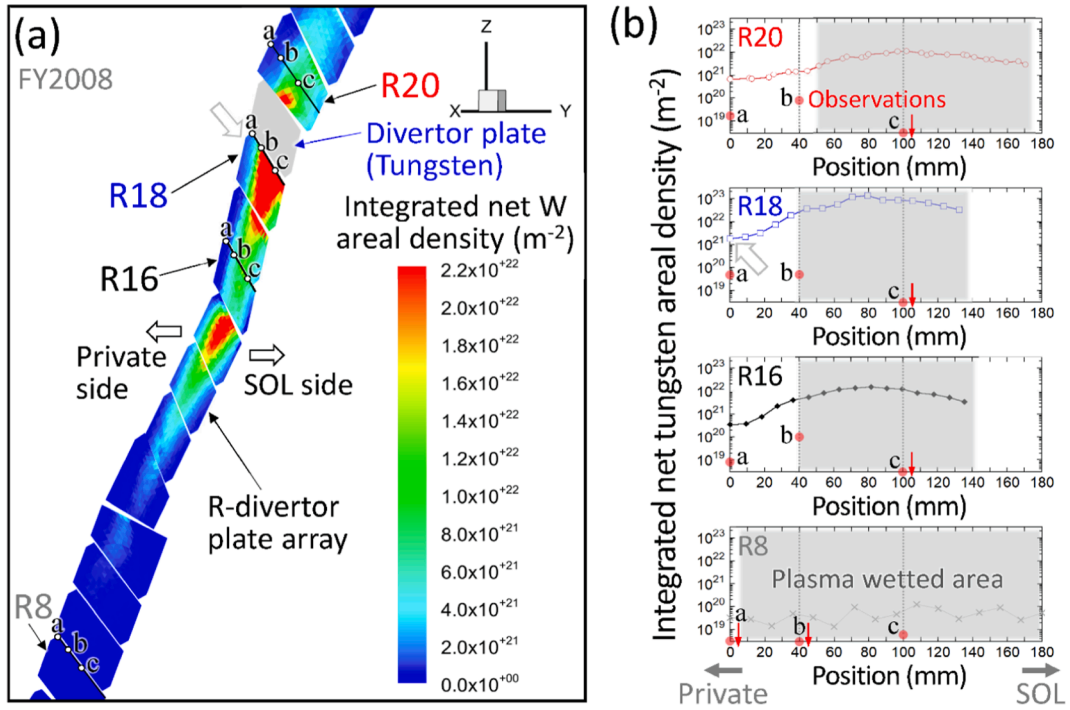


Fig. 5. (a) The simulation of the integrated net tungsten areal density profile on the carbon divertor plates installed along the right divertor plate array in the previous experimental campaign. (b) The integrated net tungsten areal density profiles along the black lines on the four carbon divertor plates, which positions are indicated in figure (a). Grey shaded areas show the plasma-wetted areas, which correspond to the erosion areas shown as blue or green on the carbon divertor plates in Fig. 4. Red circles present the measured tungsten areal densities at the three positions ("a", "b", and "c") on the four retrieved carbon divertor plates ("R20", "R18", "R16", and "R8"). (For interpretation of the references to colour in this figure legend, the reader is referred to the web version of this article.)

Table 1

Measurements of the tungsten areal density on the carbon divertor plates.

The measurements of the tungsten areal density deposited on the four retrieved carbon divertor plates ("R20", "R18", "R16", and "R8"). The measurement positions ("a", "b", and "c") are marked with small white circles along black lines on the carbon divertor plates, as shown in Fig. 5 (a). The three positions ("a", "b", and "c") correspond to the edge of the corner of the divertor plate in the private side, the positions apart from the edge by ~ 40 mm, and ~ 100 mm, respectively.

Divertor Plate	Position "a"	Position "b"	Position "c"
"R20"	$1.4 \times 10^{+19} \text{ m}^{-2}$	$8.1 \times 10^{+19} \text{ m}^{-2}$	$0.0 \times 10^{+19} \text{ m}^{-2}$
"R18"	$4.7 \times 10^{+19} \text{ m}^{-2}$	$4.8 \times 10^{+19} \text{ m}^{-2}$	$0.0 \times 10^{+19} \text{ m}^{-2}$
"R16"	$0.8 \times 10^{+19} \text{ m}^{-2}$	$10.0 \times 10^{+19} \text{ m}^{-2}$	$0.0 \times 10^{+19} \text{ m}^{-2}$
"R8"	$0.0 \times 10^{+19} \text{ m}^{-2}$	$0.2 \times 10^{+19} \text{ m}^{-2}$	$0.6 \times 10^{+19} \text{ m}^{-2}$

are consistent with the ERO2.0 simulation, as shown in the fourth column in Fig. 5 (b).

While the ERO2.0 simulations reproduced the above two measurements, there is a disagreement on the areal tungsten density at the plasma-wetted areas on the three carbon divertor plates (position "c" of "R20", "R18", and "R16" shown in Table 1 and Fig. 5 (b)). Quite low tungsten areal density was measured on the plasma-wetted areas (position "c"), which completely disagrees with the simulations as presented in grey shaded areas in Fig. 5 (b). This discrepancy indicates that the actual erosion rate of the redeposited tungsten on the carbon divertor plates by incident impurity (carbon and tungsten) ions and hydrogen ions is much higher than that in the present ERO2.0 code. The simulation showed that the erosion of the redeposited tungsten by the incident impurity ions is insignificant. The effect of the sputtering of the redeposited tungsten by charge exchange neutral hydrogen atoms, which is not included in the present ERO2.0 code, seems to be also negligible because of the low mean kinetic energy of hydrogen atoms onto the divertor plates (less than about 200 eV at most). The tungsten

ions originating from the tungsten divertor plate should arrive at the plasma-wetted areas because strong neutral tungsten line emission WI was observed on the tungsten divertor plate in plasma discharges with carbon pellet injection with a high ion temperature. Thus, the tungsten ions originating from the neutral tungsten atoms should be transported along the magnetic field lines to the plasma-wetted areas. One of the possible reasons for the discrepancy can be ascribed to the much higher erosion rate on the carbon (the base material) than the tungsten deposition rate in these areas. The redeposited tungsten on the carbon divertor plates can be eroded together with the base material. The assumption in the ERO2.0 code that the redeposited tungsten forms pure solid tungsten layers may be another reason for the discrepancy. The actual redeposited tungsten layers can be amorphous-like and contain other materials in which the sputtering yield should be much higher than that in pure solid tungsten.

The simulations of the absolute values of the integrated net tungsten areal density in the private side (position "a" and "b") on the three divertor plates ("R20", "R18", and "R16") are much larger than the measurements (shown in Table 1 and Fig. 5 (b)) by more than one order of magnitude. This observable difference suggests that the actual reflection coefficient of the redeposited tungsten on the carbon divertor plates is much higher than that in the ERO2.0 code. Another possible reason for the difference may be the microscopic exfoliation of carbon deposition layers. It has been experimentally found that the private side is a deposition dominant area where fragile carbon dominant mixed-material layers are formed during plasma discharges [17], which is consistent with the ERO2.0 simulation as shown in Fig. 4. The tungsten on the fragile carbon layers can be lost by the exfoliation of the deposition layers. Meanwhile, the code assumes that pure solid carbon layers are formed by carbon deposition, which can be inappropriate for realistic PWI simulation. In addition to this, the sputtering rate of tungsten deposited on fragile carbon layers should be higher than that deposited on pure solid carbon layers. The disagreement strongly suggests that more sophistication of the PWI model on the redeposited tungsten is

necessary for the ERO2.0 code by implementing the database on PWI given by high-performance computing [18].

Summary

The three-dimensional plasma-wall interaction simulation code ERO2.0 was applied to the analysis of the tungsten migration in the open divertor region in the LHD. The ERO2.0 simulations reproduced the measurement of the localized tungsten migration near the tungsten-coated divertor plate, which is explained by tungsten ion transport by the plasma flow along the magnetic field lines connecting to the divertor plates installed along the right divertor plate array. The simulation also qualitatively reproduced the measurement of the high tungsten areal density in the private side on a carbon divertor plate installed next to the tungsten divertor plate. The simulation revealed that the reason for the high tungsten areal density in the private side is the prompt redeposition of tungsten sputtered from the tungsten divertor plate in the plasma discharges in the low magnetic field strength in the counter-clockwise toroidal direction ($B_t = -0.50$ Tesla) for $R_{ax} = 3.60$ m. However, the simulations of the tungsten areal density on the plasma-wetted areas disagreed with the measurements, which indicates that the actual erosion rate of the redeposited tungsten is much higher than that in the present ERO2.0 code.

CRediT authorship contribution statement

M. Shoji: Supervision, Investigation, Writing – original draft, Visualization. **G. Kawamura:** Software, Resources. **J. Romazanov:** Software, Writing – review & editing. **A. Kirschner:** Software, Project administration. **S. Masuzaki:** Conceptualization, Supervision, Project administration, Funding acquisition. **M. Tokitani:** Investigation, Methodology. **S. Brezinsek:** Project administration.

Declaration of Competing Interest

The authors declare that they have no known competing financial

interests or personal relationships that could have appeared to influence the work reported in this paper.

Data availability

Data will be made available on request.

Acknowledgements

This work was performed under the auspices of the NIFS Collaboration Research program (NIFS22KIST004). The author would like to thank Y. Feng for permission to use the EMC3-EIRENE. He appreciates the computational resources of the LHD numerical analysis server and the plasma simulator in NIFS. This work is also supported by JSPS KAKENHI Grant Numbers 21K18620, 19K03802, and 18H01203, and by the Numerical Simulation Reactor Research Project (NIFS11UNTT004).

References

- [1] V. Philipps, J. Nucl. Mater. 415 (2011) S2.
- [2] R.A. Pitts, et al., Nucl. Mater. Energy 20 (2019), 100696.
- [3] Y. Takeiri, et al., Nucl. Fusion 57 (2017), 102023.
- [4] M. Tokitani, et al., Nucl. Mater. Energy 18 (2019) 23.
- [5] J. Romazanov, et al., Nucl. Mater. Energy 18 (2019) 331.
- [6] W. Möller, et al., Comput. Phys. Commun. 51 (1988) 355.
- [7] The ADAS User Manual (version 2.6) <http://adas.phys.strath.ac.uk/> (2004).
- [8] Y. Feng, et al., Plasma Phys. Control. Fusion 44 (2002) 611.
- [9] G. Kawamura, et al., Contrib. Plasma Phys. 54 (2014) 437.
- [10] G. Motojima, et al., Plasma Fusion Res. 10 (2015) 1202074.
- [11] A. Kirschner, et al., J. Nucl. Mater. 390–391 (2009) 152.
- [12] Y. Ueda, et al., Nucl. Fusion 49 (2009), 065027.
- [13] X. Yang, et al., Nucl. Instrum. Methods Phys. Res. B 308 (2013) 80.
- [14] S. Masuzaki, et al., Fusion Sci. Technol. 50 (2006) 361.
- [15] S. Masuzaki, et al., Fusion Eng. Des. 85 (2010) 940.
- [16] M. Shoji, et al., Plasma and Fusion Res. 17 (2022) 2403010.
- [17] M. Tokitani, et al., J. Nucl. Mater. 463 (2015) 91.
- [18] B.D. Wirth, et al., J. Nucl. Mater. 463 (2015) 30.